Supporting Information

An unconventional route to an ambipolar azaheterocycle and its *in situ* generated radical anion

Sarasija Das,[a] Anwesha Choudhury,[b] Arnab Mandal,[a] Chandan Kumar,[a] Smruti Ranjan Sahoo,[c] Anjan Bedi,[d] Himadri Shekhar Karmakar,[a] Nani Gopal Ghosh,[a] Somnath Dey,[e] Parameswar Krishnan Iyer,[b*] Sayan Bhattacharyya[a] and Sanjio S. Zade[a*]

[a]Department of Chemical Sciences, Indian Institute of Science Education and Research Kolkata, Mohanpur-741246, West Bengal, India. E-mail: sanjiozade@iiserkol.ac.in

[b]Department of Chemistry & Centre for Nanotechnology, Indian Institute of Technology Guwahati, Guwahati 781039, Assam, India. E-mail: pki@iitg.ac.in

[c]High Performance Computing Lab, Department of Physics, Indian Institute of Technology (ISM), Dhanbad, Jharkhand-826004, India.

[d]Institute of Chemistry, The Hebrew University of Jerusalem, Edmond J. Safra Campus, Jerusalem 91904, Israel

[e]Institute of Crystallography, RWTH Aachen University, Jägerstraße 17-19, 52066 Aachen, Germany

Table of Contents

Experimental Procedures

S1. Materials and Methods

All commercially available chemicals and reagents were purchased and used without further purification unless otherwise mentioned. Solvents like tetrahydrofuran, triethylamine, dichloromenthane, acetonitrile were dried by conventional methods, freshly distilled and stored under nitrogen. All air and water sensitive reactions were performed in oven-dried glassware using standard Schlenck techniques. 2,3-dichloroquinoxaline (1), 2,3-bisphenylehynylquinoxaline (2)[1], and (Z)-3-bromo-1-(bromo(phenyl)methylene)- 2-phenyl-1H-cyclopenta[b]quinoxaline (3)[2] were prepared according to literature procedures.

Reactions were monitored by thin layer chromatography (TLC) using Merck plates (TLC Silica Gel 60 F254). Developed TLC plates were observed under ultraviolet light (254 nm/366 nm). Silica gel (Merck) was used for column chromatography.

^{1}H NMR and ^{13}C NMR spectra were recorded on a JEOL 400 spectrometer (400 MHz for ^{1}H and 101 MHz for ^{13}C) or Bruker Avance 500 (500 MHz for ^{1}H and 126 MHz for ^{13}C) in $CDCl_3$ at room temperature. Chemical shifts (δ) are reported in ppm and were referenced to the residual undeuterated solvent signal as an internal reference ($CDCl_3$, 7.26 ppm for ^{1}H and 77.16 ppm for ^{13}C). Coupling constants (J) are given in Hz and the apparent resonance multiplicity is reported as s (singlet), d (doublet), dd (doublet of doublets), t (triplet), q (quartret), m (multiplet).

Single crystals of compounds 4 and 11 suitable for XRD analysis, were obtained by slow evaporation from their solutions in dichloromethane.

Single crystal X-ray diffraction data of crystal **4** were collected employing Mo$K\alpha$ radiation using Bruker APEX-2 CCD diffractometer. Obtained data were processed using the Bruker SAINT software package.[3] The crystal structure was solved using *SHELXT*[4] and refined using *SHELXL*[5] using the *Olex*2 graphical interface[6] (Table S3).

Single crystal X-ray diffraction experiments on crystal **11** were performed employing microfocus Cu$K\alpha$ radiation using a four circle Agilent (now owned by Rigaku) diffractometer. Single crystals were found to be severely twinned by non-merohedry [Twin matrix – (1,0,2c×cos(β)/a|0,-1,0|0,0,-1)].[7] The microscopic twin domains could not be mechanically separated. Data reduction for both components were performed using the software suite *CrysAlisPRO* in .hklf5 format.[8] The crystal structure was solved using *SHELXT*[4] and refined using *JANA*2006[9,10] in space group symmetry monoclinic (**b**–unique) $P2_1/n$ [R_F (obs) = 0.0543, Table S3].

UV-vis absorption spectrum was recorded on a JASCO V-670 spectrophotometer. HRMS data were collected using XXXaxis impact BRUKER ESI-MS instrument. TGA was carried out using a Mettler Toledo TGA/SDTA 851 thermogravimetric analyzer at a heating rate of 10 °C min^{-1} with a sample weight of ca. 2–3 mg in nitrogen atmosphere. DSC was carried out using a Mettler Toledo DSC1 STARe differential scanning calorimeter at a heating rate of 10 °C min^{-1} with a sample weight of ca. 2–3 mg in nitrogen atmosphere.

Cyclic voltammetry was performed at room temperature using dry acetonitrile as solvent, tetrabutylammonium hexafluorophosphate ($TBAPF_6$) as supporting electrolyte at a scan rate of 100 mV/s under nitrogen atmosphere. A platinum disk was used as working electrode, platinum wire was used as counter electrode and silver wire (dipped in $FeCl_3$ aqueous solution prior to use) was used as pseudo reference electrode. The potential was externally calibrated after each experiment, against the ferrocene/ferrocenium couple. Spectroelectrochemistry was performed on a JASCO V-670 UV-Vis-NIR spectrophotometer and the reduction was carried out using a Princeton Applied Research 263A Potentiostat/Galvanostat using a three-electrode setup: platinum mesh as working electrode, platinum wire as the counter electrode, and silver wire as pseudo reference electrode.

X-band EPR spectrum was recorded on a Bruker 300 spectrometer equipped with an Oxford ESR-910 liquid nitrogen cryostat.

The charge carrier mobility was measured by fabricating electron and hole only devices of the polymer and measuring the slopes from the J-V^2 plots in space charge limited current (SCLC) region. The polymer solutions were spin coated either at the top of electron transport layer (ETL, TiO_2) or hole transport layer (HTL, PEDOT:PSS). In order to determine the electron mobility (μ_e) in electron only devices, an ETL layer of TiO_2 was deposited on the top FTO substrate by spin coating at 3000 RPM for 30 s followed by thermal annealing at 550 °C for 40 min for the formation of compact TiO_2 layer. At the top of TiO_2 layer, 50 μL of compound 4 solution in chlorobenzene (30 mg/ml) was spin coated at 1000 RPM for 30 s. The process was followed again to increase the thickness of compound layer. Then substrates were transferred inside thermal evaporator for the deposition of Ag top electrode using shadow mask at a deposition rate of 1 Å/sec and base pressure of 5.0×10^{-6} Torr. The deposited film thickness of Ag was estimated by *in situ* measurement via quartz crystal thickness monitor. The hole only devices for the measurement of hole mobility (μ_h) were fabricated by following the same method, however instead of ETL, ethanolic solution of PEDOT:PSS (HTL) was deposited by spin coating at 3000 RPM for 30 s followed by heat treatment at 130 °C for 15 min.

All calculations were carried out using Gaussian 09 package.[11] The DFT method was employed using the B3LYP hybrid functional. Structures were optimized with the 6-31G(d) basis set. Nucleus independent chemical shifts (NICS) were evaluated by using the gauge invariant atomic orbital (GIAO) approach at the GIAO-B3LYP/6-311+G(d,p). NICS values were calculated as a measure of aromatic/antiaromatic character. Negative NICS value of a ring indicates the presence of induced diatropic ring current (aromatic character), whereas positive NICS value indicates the presence of induced paratropic ring current (antiaromatic character). Anisotropy of the induced current density (ACID) plot was obtained using iso-value = 0.05 and a clockwise diatropic ring current is clearly observed in the ACID plot (Figure S2(b)). The optimized structure was obtained at B3LYP/6-31G* level of theory without any imaginary frequency. Reorganization energy of the compound was then computed at similar optimization level of theory. The calculations of electronic coupling parameters such as; site energy (t), spatial overlap (S), and effective transfer integral (V_{eff}) were executed with the help of AOMix program through fragment molecular orbital approach of dimers and using PW91/6-31G* level of theory. Anisotropic charge mobility of the compound was then calculated based on the combination of Marcus-Hush theory and first-principles quantum mechanics calculation.

S2. Synthetic Details

S2.1. 7-bromo-6-phenyl-5H-8,12b-diazabenzo[a]acephenanthrylen-5-one (4)

(Z)-3-bromo-1-(bromo(phenyl)methylene)-2-phenyl-1H-cyclopenta[b]quinoxaline (920 mg, 1.88 mmol) was dissolved in 20 mL dichloromethane and stirred at room temperature in presence of anhydrous $FeCl_3$ (2.14 g, 13.16 mmol) for 24 h. Methanol was added to the reaction mixture and evaporated under reduced pressure. Flash column chromatography was performed to furnish dark violet solid of compound **4** (198 mg, 25%); melting point: 250-252 °C. ^{1}H NMR (400 MHz, $CDCl_3$) δ 8.81 (d, *J* = 8.5 Hz, 1H), 8.75 – 8.71 (m, 2H), 8.55 (dd, *J* = 8.0, 1.7 Hz, 1H), 7.97 – 7.93 (m, 2H), 7.88 – 7.77 (m, 3H), 7.71 (t, *J* = 7.7 Hz, 1H), 7.52 (m, 3H). ^{13}C NMR (126 MHz, $CDCl_3$) δ 169.62, 155.72, 153.25, 139.69, 136.89, 134.48, 132.77, 132.71, 130.98, 130.46, 130.26, 130.10, 129.88, 129.04, 128.31, 127.87, 127.08, 126.09, 120.58, 118.34, 110.57, 101.46. HRMS (ESI-TOF) m/z: $[M + H]^+$ calculated for $C_{24}H_{13}BrN_2O$, 425.0284 ; found, 425.0279.

S2.2. (Z)-3-bromo-1-(chloro(phenyl)methylene)-2-phenyl-1H-cyclopenta[b]quinoxaline (11)

Yellow solid of compound **11** was obtained as a by-product while synthesizing compound **4** in the same reaction; melting point: 167-169 °C. ^{1}H NMR (400 MHz, $CDCl_3$) δ 8.26 (m, 2H), 7.77 (m, 2H), 7.19 – 7.13 (m, 2H), 7.07 – 6.93 (m, 8H). ^{13}C NMR (126 MHz, $CDCl_3$) δ 130.55, 130.47, 130.43, 130.41, 130.19, 130.14, 129.81, 129.77, 129.65, 129.58, 129.28, 127.98, 127.92, 127.67, 127.60, 127.54. HRMS (ESI-TOF) m/z: $[M + H]^+$ calculated for $C_{24}H_{14}BrClN_2$, 445.0102 ; found, 445.0129.

S2.3. *In situ* formation of radical anion $4^{•-}$ from compound 4

The experiment was carried out in a nitrogen filled glove box. Compound **4** (10 mg, 0.024 mmol) was dissolved in a mixture of 0.7 mL dry acetonitrile in a glass vial to give a dark violet solution. In another glass vial K (1.7 mg, 0.044 mmol) was added to 18-crown-6 (11.62 mg, 0.044 mmol) and the mixture was transferred into the solution of compound 4 which immediately resulted in a dark green solution of the corresponding radical anion $\mathbf{4}^{•-}$.

Results and Discussion

Table S1. TD-DFT calculated molecular orbitals and corresponding excitations of compound **4**

State	Excitation	E_g (eV)	λ (nm)	*f*
S1	H to L (97.0%)	2.0615	602	0.0248
S2	H-1 to L (69.5%)	2.7788	446	0.1304
	H-2 to L (24.0%)			
S3	H-2 to L (70.6%)	3.0462	407	0.2292
	H-1 to L (24.2%)			

Table S2. Molecular Orbital (MO) diagrams and energies (in eV) of compound **4**

MO	Energy (eV)	Diagram
LUMO	-2.81 eV	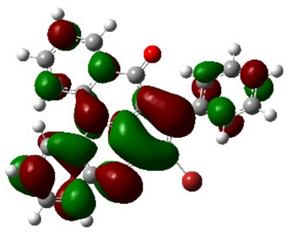
HOMO	-5.55 eV	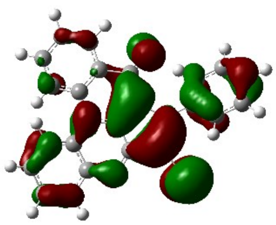

HOMO-1	-6.09 eV	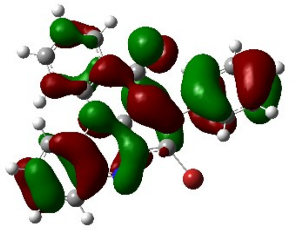
HOMO-2	-6.41 eV	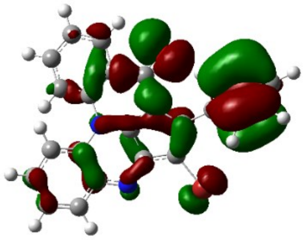

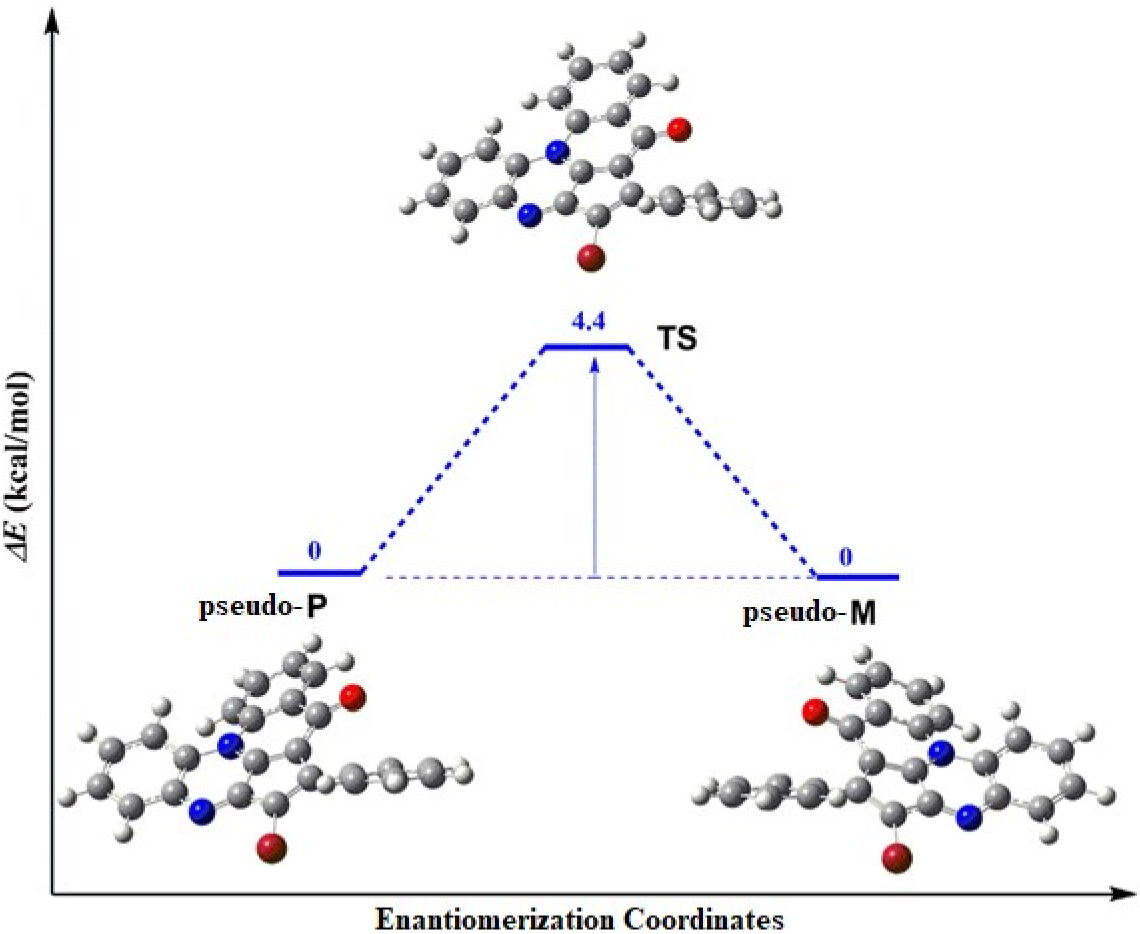

Figure S1. DFT calculated enantiomerization barrier of compound **4.**

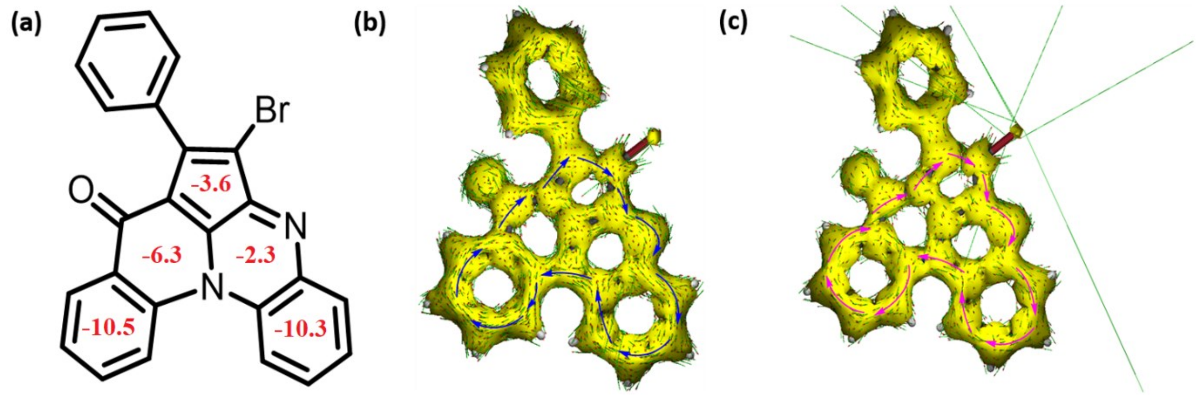

Figure S2. (a) NICS $(1)_{iso}$ values of artificially planarized compound 4 (b) ACID plot of compound **4** (c) ACID plot of radical anion **4•⁻**.

Compound **4** (empirical formula - $C_{24}H_{13}N_2OBr$) crystallizes in monoclinic (b–unique) space group *P*2$_1$/*n* [R_F^2 (obs) = 0.0488, Table S3]. Compound **11** crystallizes *P*2$_1$/*n* [R_F (obs) = 0.0543, Table S3]. Structure refinement yielded the composition of **11** to be $C_{24}H_{14}$ $Br_{(1+x)}Cl_{(1-x)}N_2$ (x = 0.287) with fully occupied bromine atom attached to the 5-membered ring, while bromine and chlorine are occupationally disordered on the exocyclic double bond with occupancy ratio Br:Cl = 0.287:0.713.

Table S3. X-ray crystallographic data of compounds **4** ($C_{24}H_{13}BrN_2O$) and **11** ($C_{24}H_{14}Br_{1.29}Cl_{0.71}N_2$)

Empirical formula	$C_{24}H_{13}BrN_2O$	$C_{24}H_{14}Br_{1.29}Cl_{0.71}N_2$
Formula weight	425.27	458.5
Temperature (K)	100	100
Wavelength (Å)	MoKα	CuKα
Crystal system	monoclinic	monoclinic
Space group	P2$_1$/n	P2$_1$/n
Crystal size (mm^3)	0.2 × 0.1 × 0.08	0.30 × 0.15 × 0.12
a (Å)	9.495(4)	9.7636(3)
b (Å)	15.107(7)	9.7605(2)
c (Å)	12.403(6)	19.7943(5)
α (°)	90	90
β (°)	93.99(2)	94.084(2)
γ (°)	90	90
Volume (Å^3)	1774.8(13)	1881.56(8)
Z	4	4
Density$_{calc}$ (g cm^{-3})	1.592	1.6186
μ (mm^{-1})	2.334	4.709
no. unique reflcns / R_{int}	4106 / 0.0982	5506 / 0.1039

no. reflcns observed [$I > 2\sigma(I)$]	2107	-
no. reflcns observed [$I > 3\sigma(I)$]	-	5153
Goodness-of-fit on F^2	0.971	-
Goodness-of-fit on F	-	3.330
R_F^2 (obs), wR_F^2 (all)	0.0488/0.0951	-
R_F (obs), wR_F (all)	-	0.0543/0.0834
$\Delta\rho$min/$\Delta\rho$max (e/Å^3)	-0.552/0.336	-1.02/1.34
CCDC	1946568	2047736

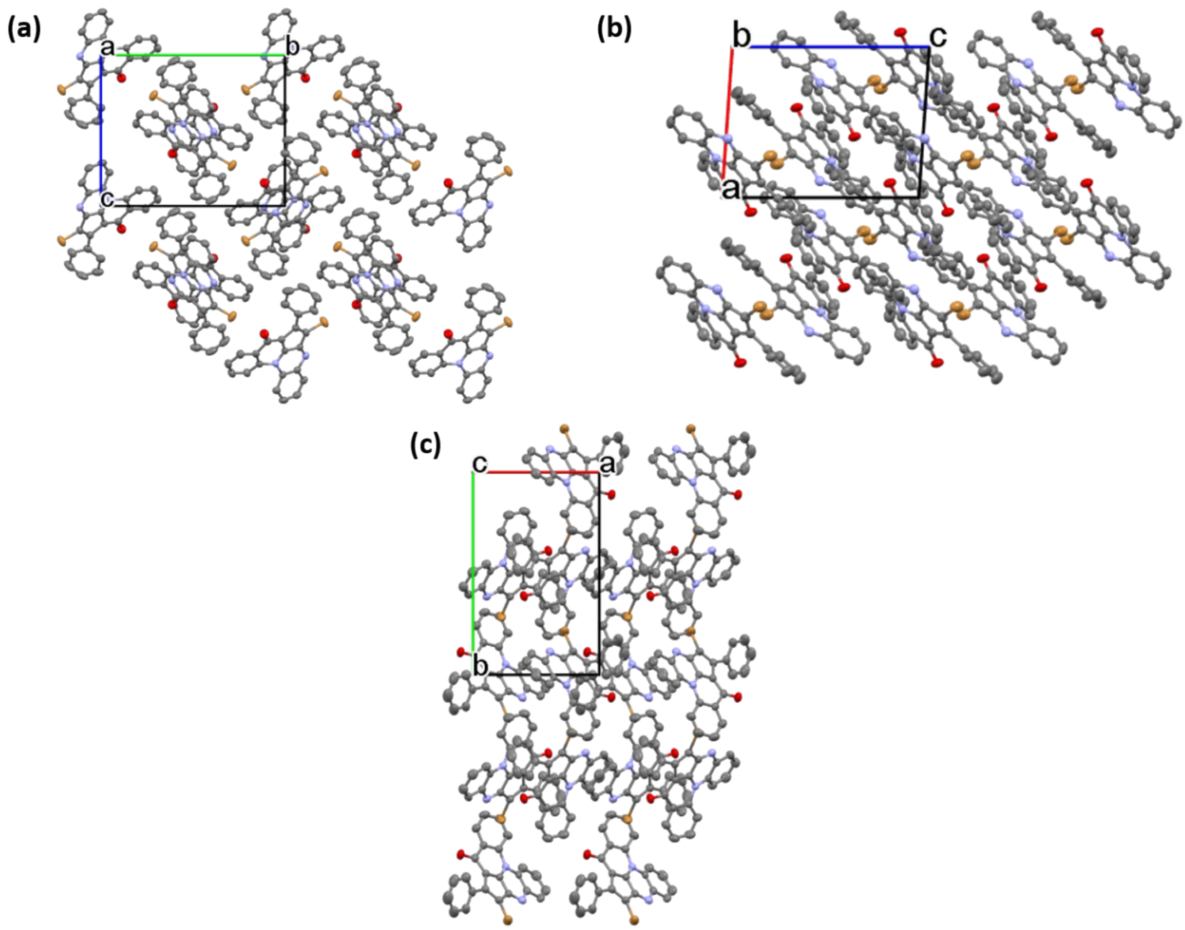

Figure S3. Packing diagram of compound 4 along (a) a-axis, (b) b-axis and (c) c-axis.

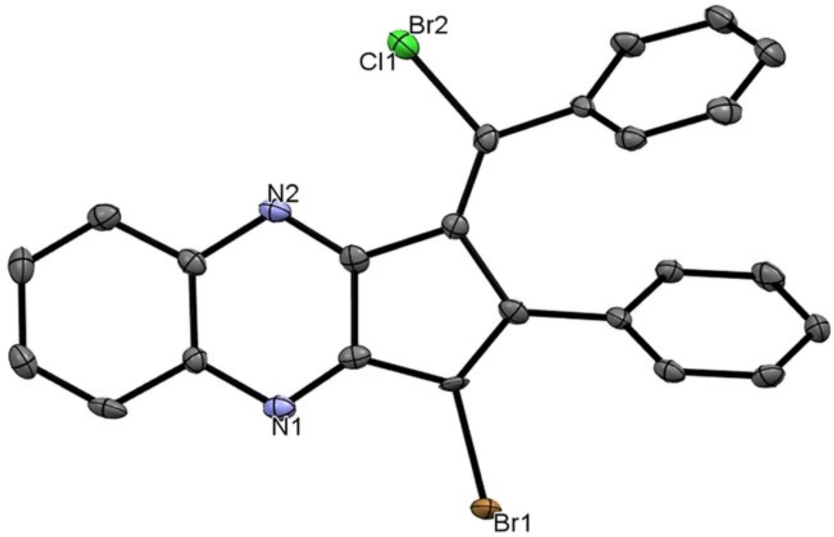

Figure S4. ORTEP diagram of compound **11** (hydrogens are omitted for clarity).

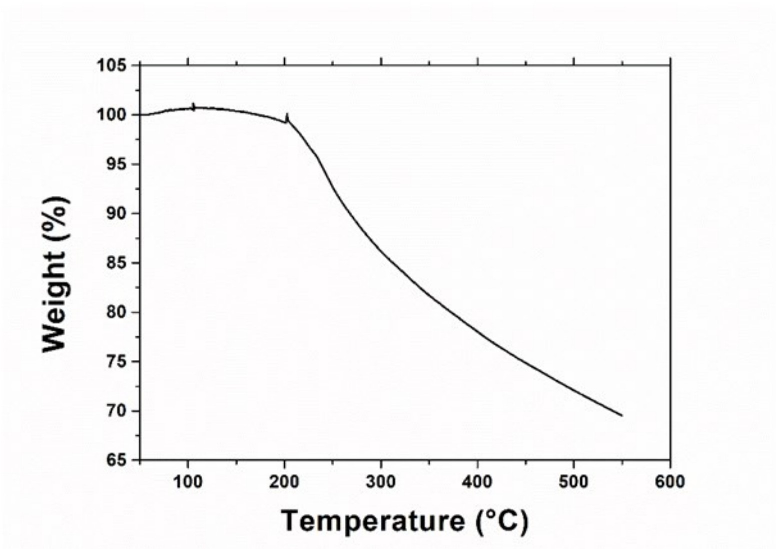

Figure S5. TGA graph of compound **4**

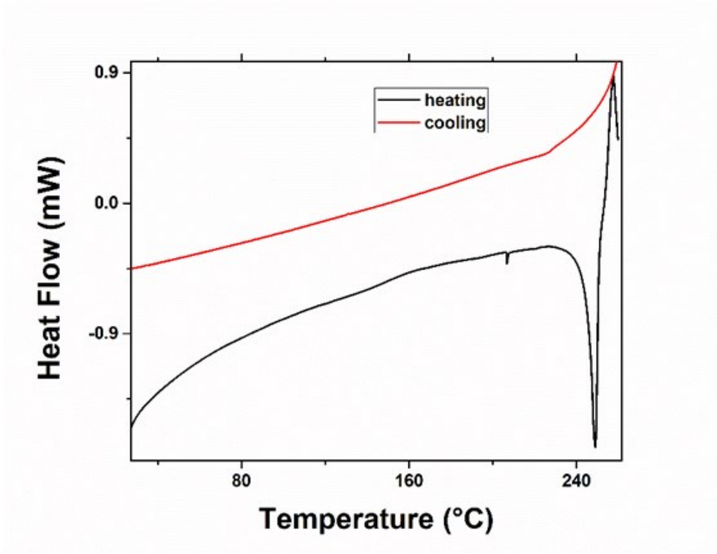

Figure S6. DSC graph of compound **4**

The electron and hole mobilities were calculated by Mott-Gurney equation.

$$J = 9\mu\varepsilon\varepsilon_o V^2/8L^3$$

where, ε is the relative dielectric constant of organic semiconductor (typically taken as 3 for small molecules), ε_o is the vacuum permittivity, e is the electron charge, L is the thickness of active layer, J is current density, μ is carrier mobility of charge carriers (electron and hole) and V is the applied voltage. The mobility of electron (μ_e) or hole (μ_h) were calculated from the slope of J vs V^2 curves.

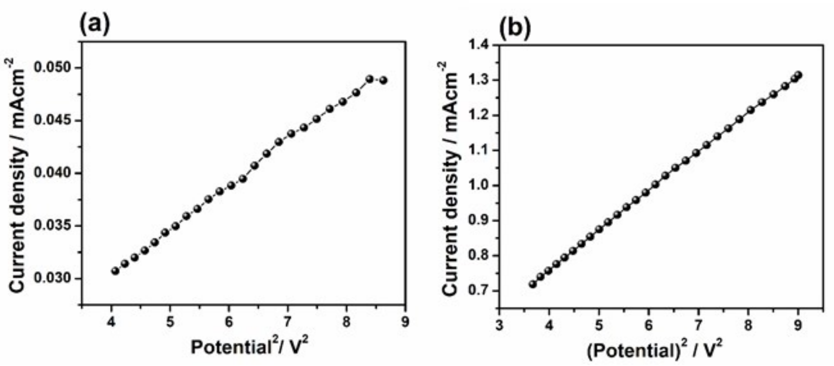

Figure S7. J-V^2 plots of devices with (a) ETL and (b) HTL under dark.

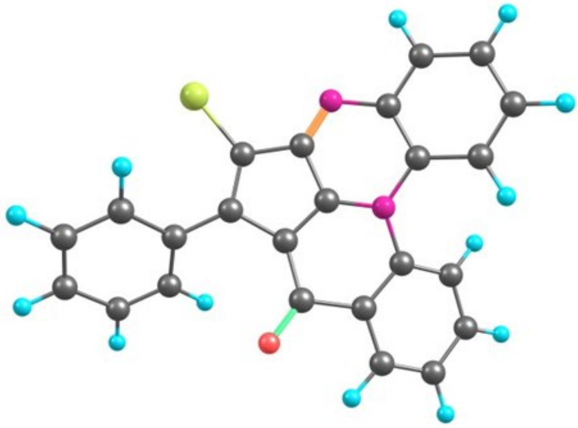

Figure S8. Optimized Structure of compound **4** (DFT-B3LYP-6-31G(d)).

The charge mobility is one of the most crucial parameters, which measure the performance of organic electronic devices. The anisotropic charge mobilities of the organic crystals were predicted based on the combination of first-principles quantum mechanics calculations and Marcus-Hush theory.[12] At room temperature, the intermolecular charge transfer rate (K) from the Marcus-Hush theory can be written as;

$$K = \frac{V^2}{\hbar}\left(\frac{\pi}{\lambda k_B T}\right)^2 \exp\left(-\frac{\lambda}{4k_B T}\right)\cdots\cdots(1)$$

where V, k_B, and λ are the electronic coupling, Boltzmann constant, and reorganization energy, respectively.

For organic semiconductors, when the electron-vibration coupling is far more than intermolecular coupling, in that case it is seen that, in order to explain the charge transport mechanism, the hopping model is more successful as compared to the band model.[13–15]

Based on the molecular molecular orbitals of conjugated organic compounds, the intermolecular effective electronic coupling, V_{eff} for hole (h) or electron (e) (${V_{eff}}^{h/e}$) can be determined by using the *direct coupling* (DC) method as;

$${V_{eff}}^{h/e} = \frac{J_{\alpha\beta} - {}^1/_2 S_{\alpha\beta}(t^{H/L}_{\alpha\alpha} + t^{H/L}_{\beta\beta})}{1 - S^2_{\alpha\beta}}\cdots\cdots(2)$$

where $J_{\alpha\beta}$ and $S_{\alpha\beta}$ are called as charge transfer integrals and spatial overlaps, respectively.[12,16–19] The parameters $t^{H/L}_{\alpha\alpha}$ and $t^{H/L}_{\beta\beta}$ are defined as the site energies contributed from highest occupied molecular orbitals (HOMO) and lowest unoccupied molecular orbitals (LUMO) respectively.[12,16-19] In *direct coupling*, the electron dimer states are specified in terms of localized monomer orbitals and the charge-localized monomer diabatic states.[19]

For the dimer system, with Kohn-Sham Hamiltonian, H_{KS}, and with $t^{H/L}_{\alpha}$ and $t^{H/L}_{\beta}$ being HOMO or LUMO of two constituting monomers α and β, the above specified terms can be determined as;[16,17]

$$J_{\alpha\beta} = \langle \varphi^{H/L}_{\alpha} | H | \varphi^{H/L}_{\beta} \rangle \cdots\cdots (3)$$

$$S_{\alpha\beta} = \langle \varphi^{H/L}_{\alpha} \mid \varphi^{H/L}_{\beta} \rangle \cdots\cdots (4)$$

$$t_{\alpha\alpha} = \langle \phi^{H/L}_{\alpha} | H_{KS} | \phi^{H/L}_{\alpha} \rangle \text{L L } (5)$$

$$t_{\beta\beta} = \langle \varphi^{H/L}_{\beta} | H_{KS} | \varphi^{H/L}_{\beta} \rangle \cdots\cdots (6)$$

At room temperature, considering the diffusive behaviour of charge transfer between the adjacent molecules of organic crystal, the isotropic drift mobility of the organic crystal by following the Einstein-Smonluchowski relation, can be given by;[12,16,17]

$$\mu = \frac{e}{k_B T} D \cdots\cdots (7)$$

where D is known as isotropic charge diffusion coefficient, and is written as follows;

$$D = \frac{1}{2n} \sum_i r_i^2 . K_i . P_i \cdots\cdots (8)$$

n is spatial dimensionality, r_i is the intermolecular distance for ith hopping pathway, and P_i defines the hopping probability which is calculated in terms of charge hopping rate as;

$$P_i = \frac{K_i}{\sum K_i} \cdots\cdots (9)$$

For organic crystals, the value of anisotropic charge mobility are calculated in a certain direction, which depends on the orientation of the crystals. Hence, we analyze the mobility of the studied organic crystals in a specific surface for each directions in terms of crystallographic plane of interest ($K_i . r_i . \cos \gamma_i$). Further, considering the orientation angle, Φ and conduction angle, θ_i with respect to the reference axis (a, b, or c); the angular-anisotropic charge carrier mobility can then be deduced from the relation;[12]

$$\mu_{\Phi} = \frac{e}{2k_B T} \sum_i K_i . r_i^2 . P_i . \cos^2 \gamma_i \cos^2 (\theta_i - \Phi) \cdots\cdots (10)$$

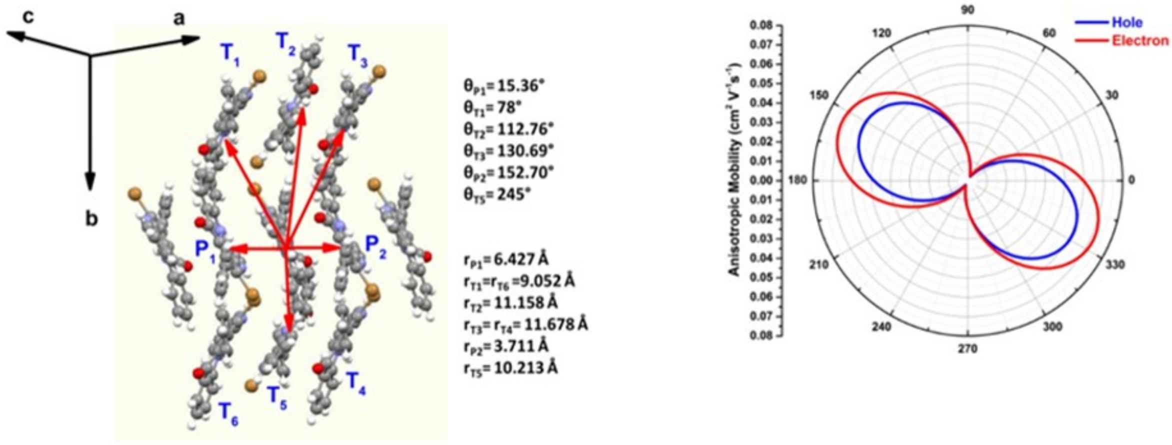

Figure S9. (a) Different hopping pathways with intermolecular distances and values of the conduction angles with respect to the crystallographic reference axis and (b) predicted angular anisotropic charge carrier mobilities of the compound.

The molecular packing mode is of great importance for the electronic coupling and charge transport in conjugated organic crystals.[17,18,20] The molecular packing modes along with all nearest possible projected hopping pathways of the studied crystals are displayed in Figure S7(a). It is clear from the Figure S7(a) that the packing structure of the investigated compound show herringbone patterns and we noticed only two types of dimers in the crystal such as, parallel (P) or face-to-face and transverse (T) or edge-to-edge dimers. The values of hopping distances between the dimers and the conduction angles with respect to reference axes of the crystal are depicted in Figure S4. The intermolecular distances corresponding to the hopping pathways P_1, T_1, T_2, T_3, P_2, and T_5 are denoted as r_{P1}, r_{T1}, r_{T2}, r_{T3}, r_{P2}, and r_{T5} and the corresponding hopping angles are θ_{P1}, θ_{T1}, θ_{T2}, θ_{T3}, θ_{P2}, and θ_{T5} respectively.

The computed values of spatial overlap (S), site energy (t), and effective transfer integral (V_{eff}) of the crystals at PW91/6-31G* level of theory are summarized in the Table S4. It is known that, smaller intermolecular distance and parallel packings are the two crucial factors for larger electronic coupling (V). For example, the P_2 pathway with hopping distance 3.711 Å resulted the largest effective electronic coupling V_{eff}^h (for hole) and V_{eff}^e (for electron) values such as 54.60 meV and 53.20 meV, respectively. These values are due to maximum spatial overlap between the molecular orbital in the P_2 direction. Similarly, the P_1 pathway possess the V_{eff}^h and V_{eff}^e values such as -13.70 meV and -22.50 meV, and the intermolecular hopping distance, 6.427 Å. Further, among all the transverse dimers, T_1 dimer possesses larger V_{eff}^h value as 15.40 meV. From the electronic coupling calculations, it is clear that, we can predict the similar value of the hole and electron mobilities for the compound.

Table S4. Calculated spatial overlap (S), site energy (t), effective transfer integral (V_{eff}) and the range of simulated angular anisotropic hole and electron mobility of compound 4

Dimers	V_{eff}^h / V_{eff}^e (meV)	$S_{\alpha\beta}^h$ /$S_{\alpha\beta}^e$	$t_{\alpha\alpha}^h$ / $t_{\alpha\alpha}^e$ (eV)	$t_{\beta\beta}^h$ / $t_{\beta\beta}^e$ (eV)	μ_Φ^h / μ_Φ^e (cm^2 $V^{-1}s^{-1}$)
P1	-13.70/-22.50	0.0015/0.003	-4.956/3.384	-4.956/-3.384	(0.0025 - 0.061) / (0.0029 - 0.072)
T1	15.40/-1.30	-0.0017/0.0002	-4.862/-3.328	-4.757/-3.223	
T2	-0.50/6.30	0.0001/-0.0009	-4.827/-3.285	-4.907/-3.352	
T3	0.60/0.30	-0.0001/0.0	-4.807/-3.278	-4.827/-3.289	
P2	54.60/53.20	-0.0074/-0.0053	-4.784/-3.130	-4.784/-3.130	
T5	0.70/-0.50	0.0/0.0	-4.765/-3.231	-5.109/-3.553	

The anisotropic charge mobility of the studied compound is calculated in a particular transistor channel which depends on the specific surface of the crystal. Considering the reorganization energies and the effective intermolecular electronic coupling, the anisotropic charge mobilities were simulated by using the angular anisotropic mobility equation, and shown in Figure S4 and values are listed in the Table S4. As it is already discussed, the maximum angular hole and electron mobilities were noticed in directions of smaller hopping distances and for face-to-face parallel packing pathways due to large hole and electron intermolecular coupling. From simulation, the maximum hole ($\mu_\Phi{}^h$) and electron ($\mu_\Phi{}^e$) mobility of the studied compound were found in P_2 direction and the values are 0.061 $cm^2V^{-1}s^{-1}$ at the angle Φ=152.41°/332.32° and 0.072 $cm^2V^{-1}s^{-1}$ at Φ=155.27°/335.18°, respectively. Similarly, the minimum $\mu_\Phi{}^h$ and $\mu_\Phi{}^e$ values were found to be 0.0025 $cm^2V^{-1}s^{-1}$ at Φ=62.45°/242.36° and 0.0029 $cm^2V^{-1}s^{-1}$ at Φ=65.32°/245.23°, respectively. Further, for T_1 hopping path, the calculated $\mu_\Phi{}^h$ and $\mu_\Phi{}^e$ for the compound were obtained as 0.007 $cm^2V^{-1}s^{-1}$ and 0.0061 $cm^2V^{-1}s^{-1}$ at Φ=78°, respectively. Since, the reorganization energies (0.359 eV for hole and 0.341 eV for electron) and electronic couplings valuess of both hole and electron are nearly similar, respectively; hence, there is no significant deviation is observed in between the predicted angular anisotropic hole and electron mobilities of the studied compound.

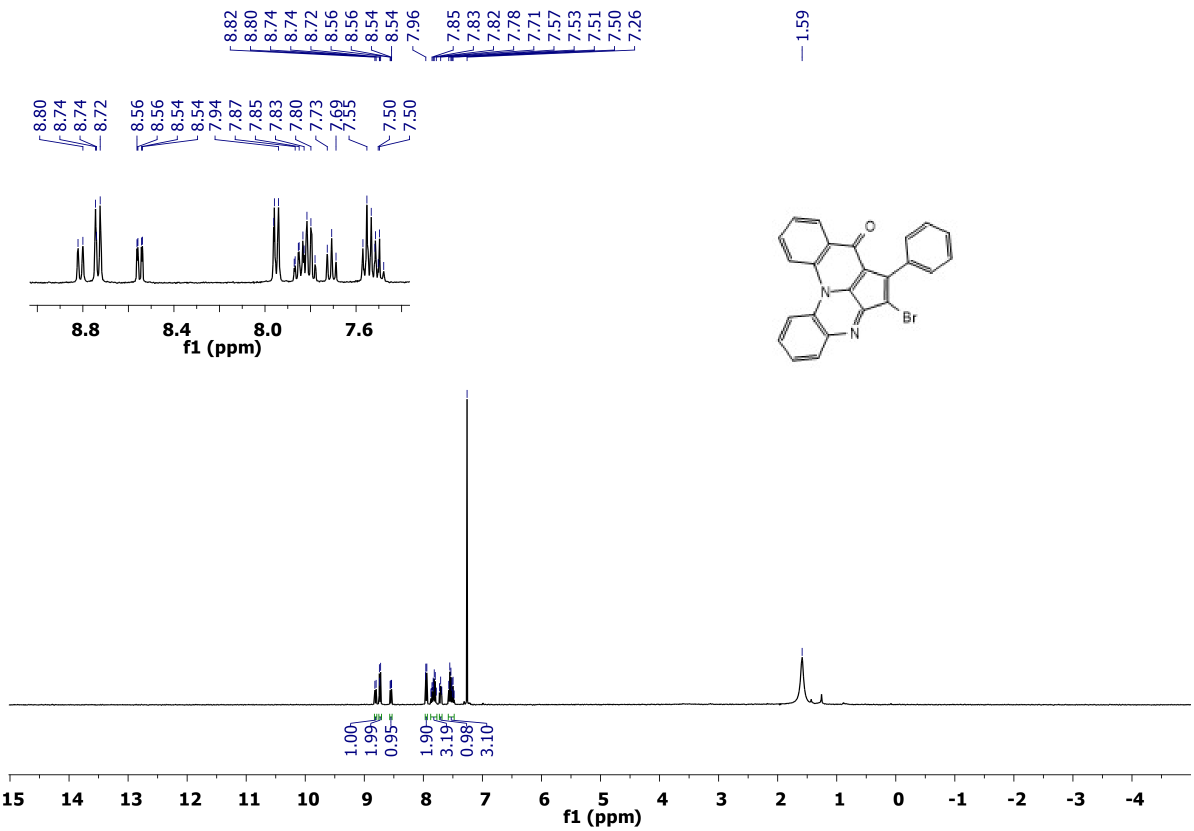

Figure S10. ^{1}H NMR spectrum of compound **4**.

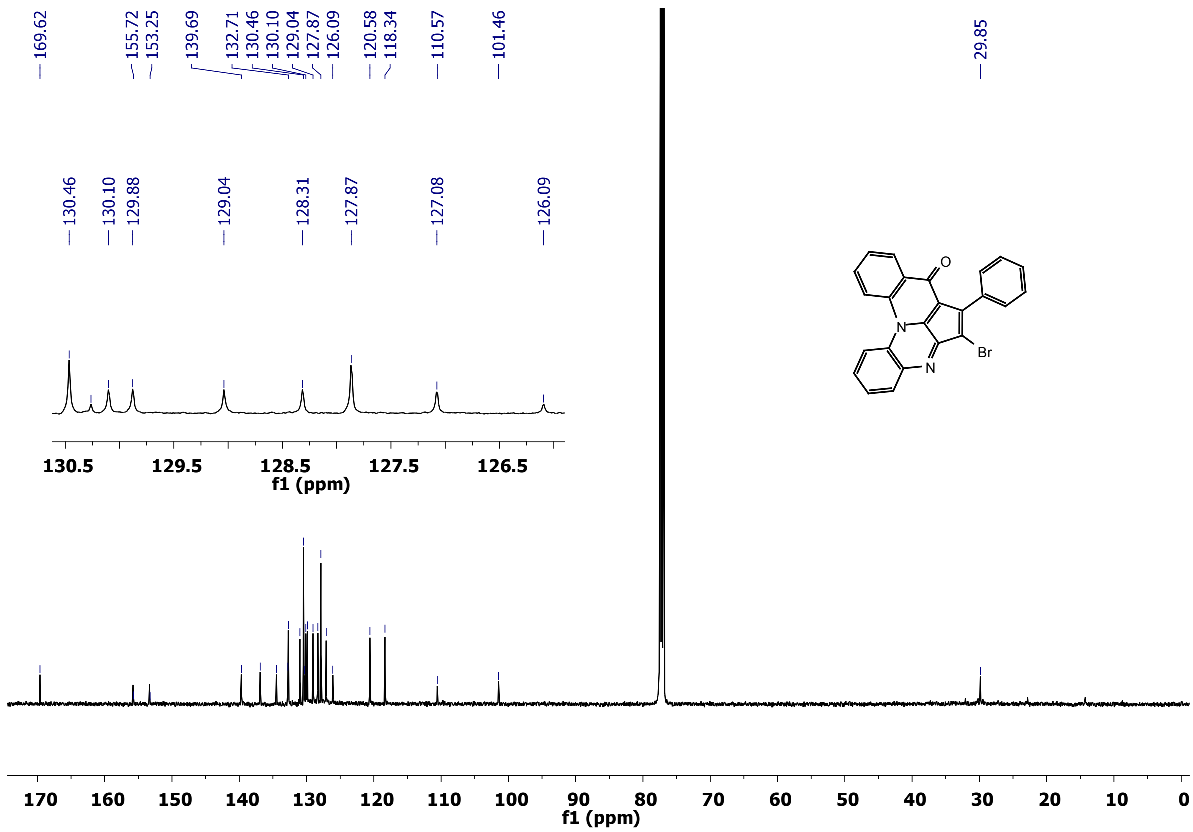

Figure S11. ^{13}C NMR spectrum of compound **4**.

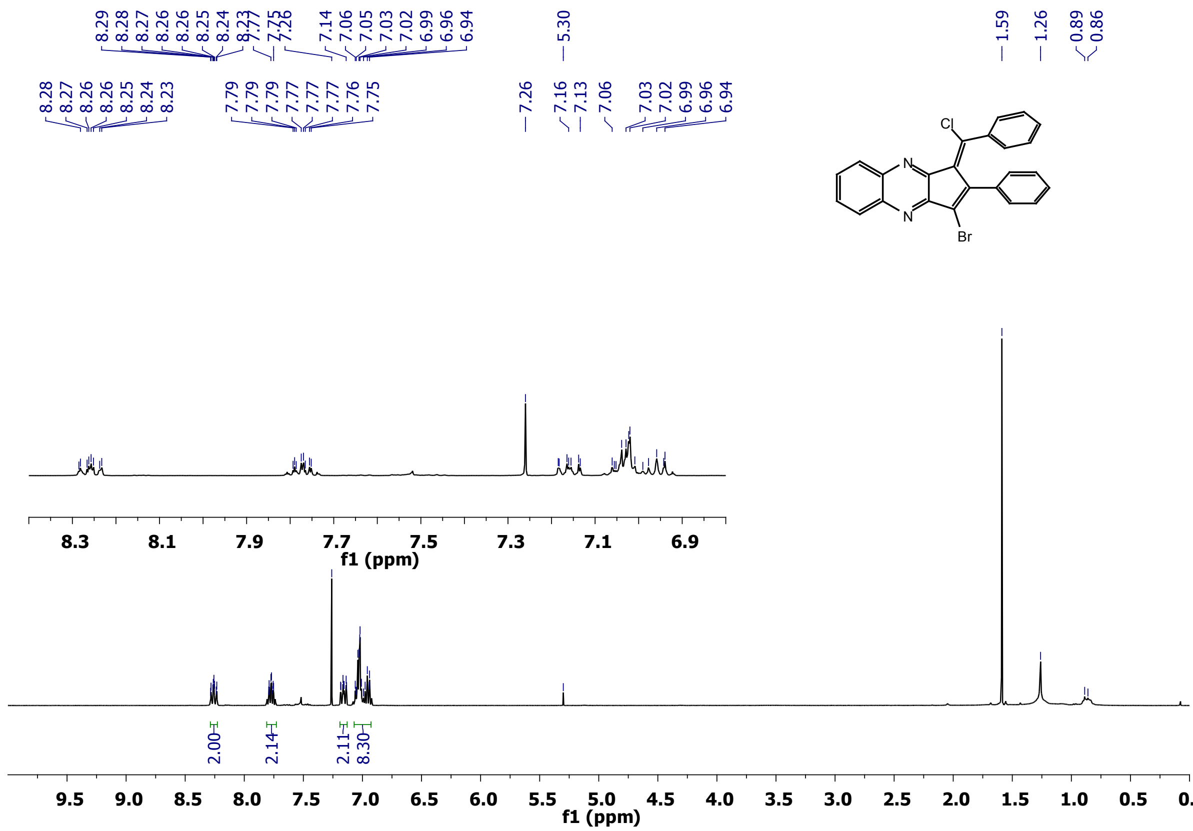

Figure S12. [1]H NMR spectrum of compound **11**.

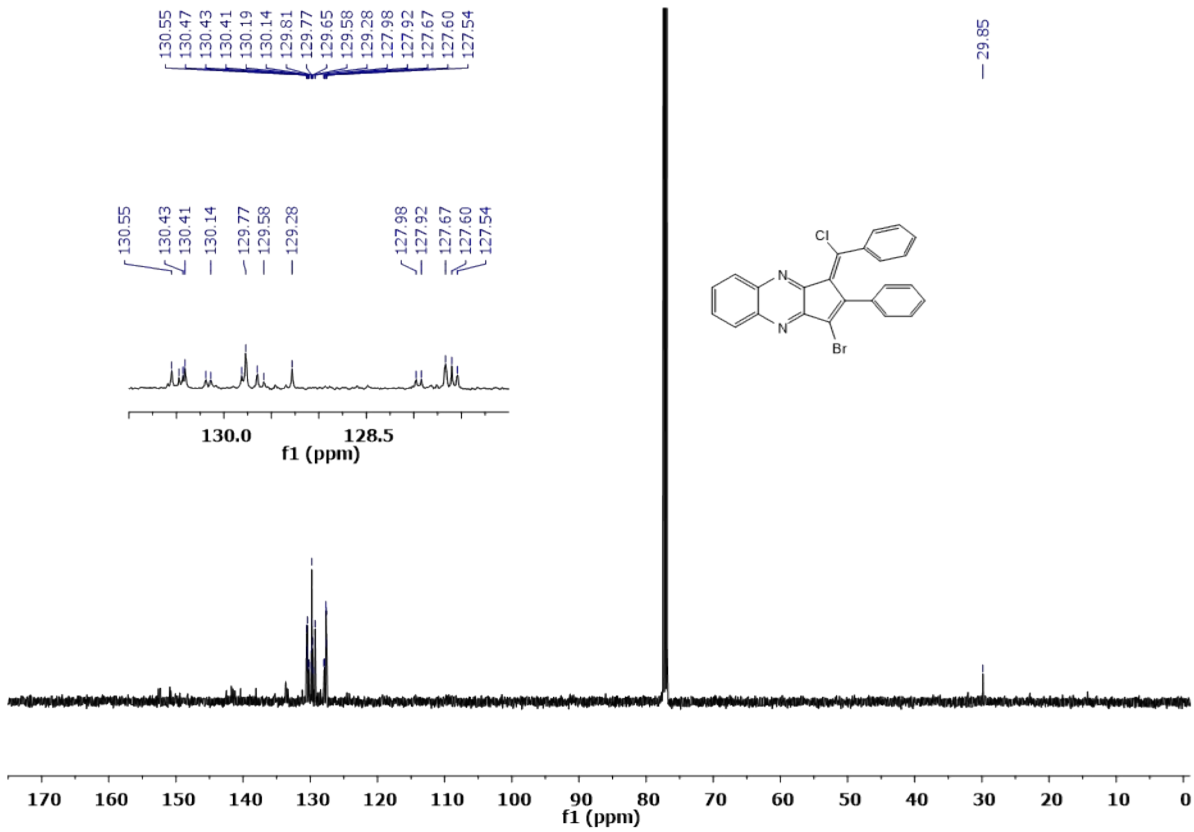

Figure S13. [13]C NMR spectrum of compound **11**.

References

1 A. V Gulevskaya, S. Van Dang, A. S. Tyaglivy, A. F. Pozharskii, O. N. Kazheva, A. N. Chekhlov and O. A. Dyachenko, *Tetrahedron*, 2010, **66**, 146–151.

2 A. V Gulevskaya, R. Y. Lazarevich and A. F. Pozharskii, *Tetrahedron*, 2013, **69**, 910–917.

3 V. SAINT-Plus, *Madison, WI*.

4 G. M. Sheldrick, *Acta Crystallogr. Sect. A*, 2015, **71**, 3–8.

5 G. M. Sheldrick, *Acta Crystallogr. Sect. C*, 2015, **71**, 3–8.

6 O. V Dolomanov, L. J. Bourhis, R. J. Gildea, J. A. K. Howard and H. Puschmann, *J. Appl. Crystallogr.*, 2009, **42**, 339–341.

7 S. Parsons, *Acta Crystallogr. Sect. D*, 2003, **59**, 1995–2003.

8 Agilent Technologies, *Technol. UK Ltd, Yarnton, Oxford, UK*, 2014.

9 V. Petříček, M. Dušek and L. Palatinus, *Zeitschrift für Krist. - Cryst. Mater.*, 2014, **229**, 345–352.

10 V. Petříček, M. Dušek and J. Plášil, *Zeitschrift für Krist. - Cryst. Mater.*, 2016, **231**, 583–599.

11 M. J. Frisch, G. W. Trucks, H. B. Schlegel, G. E. Scuseria, M. A. Robb, J. R. Cheeseman, G. Scalmani, V. Barone, B. Mennucci, G. A. Petersson, H. Nakatsuji, M. Caricato, X. Li, H. P. Hratchian, A. F. Izmaylov, J. Bloino, G. Zheng, J. L. Sonnenberg, M. Had, D. J. Fox, M. J. Frisch, G. W. Trucks, H. B. Schlegel, G. E. Scuseria, M. A. Robb, J. R. Cheeseman, G. Scalmani, V. Barone, B. Mennucci, G. A. Petersson, H. Nakatsuji, M. Caricato, X. Li, H. P. Hratchian, A. F. Izmaylov, J. Bloino, G. Zheng, J. L. Sonnenberg, M. Hada, M. Ehara, K. Toyota, R. Fukuda, J. Hasegawa, M. Ishida, T. Nakajima, Y. Honda, O. Kitao, H. Nakai, T. Vreven, J. A. Montgomery Jr., J. E. Peralta, F. Ogliaro, M. Bearpark, J. J. Heyd, E. Brothers, K. N. Kudin, V. N. Staroverov, R. Kobayashi, J. Normand, K. Raghavachari, A. Rendell, J. C. Burant, S. S. Iyengar, J. Tomasi, M. Cossi, N. Rega, J. M. Millam, M. Klene, J. E. Knox, J. B. Cross, V. Bakken, C. Adamo, J. Jaramillo, R. Gomperts, R. E. Stratmann, O. Yazyev, A. J. Austin, R. Cammi, C. Pomelli, J. W. Ochterski, R. L. Martin, K. Morokuma, V. G. Zakrzewski, G. A. Voth, P. Salvador, J. J. Dannenberg, S. Dapprich, A. D. Daniels, Ö. Farkas, J. B. Foresman, J. V Ortiz, J. Cioslowski and D. J. Fox, *Gaussian Inc., Wallingford*, 2013.

12 W.-Q. Deng, L. Sun, J.-D. Huang, S. Chai, S.-H. Wen and K.-L. Han, *Nat. Protoc.*, 2015, **10**, 632–642.

13 Y. C. Cheng, R. J. Silbey, D. A. da Silva Filho, J. P. Calbert, J. Cornil and J. L. Brédas, *J. Chem. Phys.*, 2003, **118**, 3764–3774.

14 X. Zhang, X. Yang, H. Geng, G. Nan, X. Sun, J. Xi and X. Xu, *J. Comput. Chem.*, 2015, **36**, 891–900.

15 S. Mohakud and S. K. Pati, *J. Mater. Chem.*, 2009, **19**, 4356–4361.

16 S.-H. Wen, A. Li, J. Song, W.-Q. Deng, K.-L. Han and W. A. Goddard, *J. Phys. Chem. B*, 2009, **113**, 8813–8819.

17 J.-D. Huang, S.-H. Wen, W.-Q. Deng and K.-L. Han, *J. Phys. Chem. B*, 2011, **115**, 2140–2147.

18 C.-H. Kuo, D.-C. Huang, W.-T. Peng, K. Goto, I. Chao and Y.-T. Tao, *J. Mater. Chem. C*, 2014, **2**, 3928–3935.

19 J.-D. Huang, W.-L. Li, S.-H. Wen and B. Dong, *J. Comput. Chem.*, 2015, **36**, 695–706.

20 S. E. Koh, C. Risko, D. A. da Silva Filho, O. Kwon, A. Facchetti, J.-L. Brédas, T. J. Marks and M. A. Ratner, *Adv. Funct. Mater.*, 2008, **18**, 332–340.